Alteration of 29Si-doped SON68 borosilicate nuclear waste glass in the presence of near field materials

Rachid Bouakkaz, Abdesselam Abdelouas, Yassine El Mendili, Karine David, Bernd Grambow

Alteration of ^{29}Si-doped SON68 borosilicate nuclear waste glass in the presence of near field materials

Rachid Bouakkaz, Abdesselam Abdelouas*, Yassine El Mendili, Karine David, Bernd Grambow

SUBATECH – IMT Atlantique-CNRS/IN2P3-Université de Nantes, 4 rue Alfred Kastler – La Chantrerie, B.P. 20722, 44307 Nantes cedex 03, France

*corresponding author: abdesselam.abdelouas@subatech.in2p3.fr

Abstract

The leaching of ^{29}Si-doped SON68 French nuclear waste glass was investigated in Callovo-Oxfordian (COx) water in the presence of P235GH stainless steel and COx argillite. Experiments were carried out to understand the effect of near-field materials on the rate of glass dissolution and the migration of ^{29}Si in the claystone core. Tests were performed by using percolation cells containing glass and stainless steel sandwiched between two clay cores in two different combinations: glass/clay at 50 and 90°C, and glass/steel/clay/ at 90°C. COx water was injected through the percolation cells at 120 bars (solution flow rate 0.05–0.38 mL d^{-1}). Results showed that the presence of steel did not enhance the dissolution rate of the glass despite the retention of ^{29}Si released from the glass on the corrosion products. The glass dissolution rate up to 17 months tends towards 10^{-4} and 10^{-3} g m^{-2} d^{-1} at 50 and 90°C, respectively. The glass alteration in the presence of clay leads to the formation of calcite and Mg-silicates at 50°C in addition to apatite and powellite at 90°C. The main steel corrosion products were siderite, magnetite, ferrosilicates, pyrite, pyrrhotite, troilite and mackinawite. $MgSO_4$ and $CaSO_4$ were also identified in the presence of steel.

Keywords: SON68 glass, carbon steel, nuclear waste disposal, corrosion, Raman spectroscopy

1. Introduction

In the deep geological repository concept for the disposal of French high-level nuclear waste glass R7T7 developed by Andra (National Radioactive Waste Management Agency), the glass is encased in a stainless steel container. The latter is then placed in a steel overpack to be stored in a multi-barrier underground disposal facility located in an argillaceous Callovo-Oxfordian (COx) layer. The overpack walls, which are 55 mm thick, protect the nuclear glass from contact with groundwater during the first thousand years, where the temperature of the package is expected to reach up to about 90°C. Void spaces around the disposed waste package may remain open for some thousands of years leading to corrosion of the overpack by vapor and by accessing clay pore water. After the rupture of the overpack containers by corrosion and geomechanical constraints, the glass would become directly in contact with their corrosion products and potentially as well the claystone host rock. These materials, also called Near-Field (NF) Materials, could interact with the glass and thus modify its long-term corrosion kinetics and associated mechanisms.

Indeed, the dissolution rate of the glass is directly related to the chemistry of the surrounding solution, especially the silicon concentration, but also to the properties of the gel formed at glass surface [1]. Firstly, the steel corrosion could occur under oxidizing conditions. But quickly, and following the oxygen consumption, the environment evolves towards reducing conditions. The steel corrosion by vapor and clay pore water should therefore occur under predominantly reducing conditions. The main products that are expected to form are iron oxides and iron carbonates [2] as well as hydrogen gas, which may reduce the oxidized forms of radionuclides [3]. The nature of the solid corrosion products depends on the pH, temperature, relative humidity, pCO_2, redox potential of the surrounding medium and microbial activity [4][5][6][7]. Numerous experiments have been carried out on the alteration of the glass/iron system [2]; the glass in the presence of $FeCl_2$ and $FeCl_3$ [8] and the glass/corrosion products system [4]. These studies revealed an increase in glass alteration in the presence of iron whatever its form. Two major mechanisms are envisaged to explain this increase: (1) the sorption of silica on corrosion products [9][10], and (2) the formation of iron silicate [11][12]. The formation of iron corrosion products and the release of iron into the near field environment can also modify the transport properties of the medium such as permeability and porosity and affect the migration of radionuclides.

Like steel, the clay can also interact with the elements released from the glass especially silicon, which may change the chemistry of the surrounding solution and form other solid phases [13]. Consequently, the formation of the gel protective layer at glass surface will be delayed [14] and the glass alteration can then continue at a high leaching rate over longer periods. On the other hand, Lemmens [15] showed that in the presence of clay at high concentrations, the dissolution rate of the SON68 glass decreases. The concentration of silica at saturation conditions was higher in the presence of clay than in aqueous environments that does not initially contain clay.

The objective of the present experimental study is to determine the impact of both COx claystone and P235GH steel corrosion products on the behaviour of silica released from SON68 glass and the leaching rate of the glass. To do so, we simulated the glass alteration in confined multi-barrier repository environment. Well-adapted percolation cells containing two clay cores were used and ^{29}Si-doped SON68 glass was chosen to allow isotopic tracing of this target element in the leachate. Three systems were studied: (Glass–Clay–50°C, also named G–C–50°C); (Glass–Clay–90°C, also named G–C–90°C) and (Glass–Steel–Clay –90°C, also named G–S–C–90°C). The long-term glass corrosion kinetic in such an environment was determined and compared to that obtained in aqueous medium under silica saturated conditions. Solid analyses were also carried out to identify the different phases formed at the different interfaces.

2. Experimental

2.1. Materials and methods

Glass alteration experiments were carried out with a ^{29}Si-doped inactive simulated French nuclear waste glass SON68 ([^{29}Si] = 14%; corresponding to ^{29}Si/^{28}Si ratio of 0.16). The composition of this glass is listed in Table 1. The glass provided in block by the French Alternative Energy and Atomic Energy Commission (CEA) was cut into thin monoliths with dimensions of (7 × 7 × 0.9 mm) and polished with finally 1 µm diamond paste. Furthermore, another fraction of the glass was ground and dry sieved to 32 µm <Φ <100 µm. Glass powder and monoliths were carefully washed with ethanol during 1 h in an ultrasound device in order to remove glass fines. The geometric surface area was calculated from the average grain size using McGrail et al. [16] relationship and by assuming spherical grains:

$$S_{geo} = (3/\rho \times r) \quad (1)$$

where S_{geo} is the surface area ($m^2\ g^{-1}$), ρ is the glass density (2.63 g cm^{-3}) and r is the average radius (m). The calculated geometric surface area gives a value of 0.047 $m^2\ g^{-1}$. P235GH stainless steel powder ($32 < \Phi < 125$ μm) and monoliths ($7 \times 7 \times 0.9$ mm) were prepared using the same method as used for the glass. The steel composition is shown in Table 2.

Synthetic Callovo-Oxfordian (COx) pore waters were prepared according to the procedure described by Gaucher et al. [17]. The chemical composition of pore waters, in equilibrium with the clay stone at different temperatures, is given in Table 3.

Percolation experiments were carried out in identical stainless steel cells, each cell has an inner diameter of 21.2 mm and a length of 42 mm. Two COx argillite cores with a diameter of 21 mm and 19 mm length were placed in each cell. The cores were machined from the initial COx core sampled in the underground research laboratory of Bure (Meuse/Haute-Marne), located at 490 m deep. COx argillite is made of 45-50% of clay fraction made of 10-24% of interstratified illite-smectite, 17-21% illite, 3-5% kaolinite and 2-3% chlorite in addition to quartz, calcite and other minor phases [18]. To study the system (G–C–S–90 °C), glass and steel were sandwiched between two clay cores (Fig. 1). The system in the cell is configured as follows:

• Clay core (19 mm length).
• 0.5 g of P235GH steel powder ($32 < \Phi < 125$ μm) with 0.6 mm in thickness
• 2 steel monoliths + 2 glass monoliths (0.7cm × 0.7cm × 0.9mm) polished to 3μm.
• 1 g of glass powder ($32 < \Phi < 100$ μm) with 1 mm in thickness.
• (2 steel monoliths + 2 glass monoliths) in a crossed position compared to the previous ones (with 0.9 mm in thickness)
• 0.5 g of P235GH steel powder ($32 < \Phi < 125$ μm) with 0.6 mm in thickness.
• Clay core (19 mm length).

The same configuration was used for the system (G–C) at 50 and 90°C without addition of steel. The volume of water available in our experiments was difficult to analyze given that the claystone cores are only slightly porous and there is a pressure gradient. In calculations involving normalized leaching rates, we assumed a water volume of 2 mL (compared with the clay rock volume of about 14 mL) which corresponds to an upper limit of porosity of 17% for the Callovo-Oxfordian claystone [19]. Neeway [20] tested this assumption by arbitrarily

adjusting the volume from 0.5 to 4 mL to see the volume effect of release rate. The author found that for long time periods the effect on release rate was non-existent.

Hence, the volume of solution in contact with the glass in each experiment (1g having a surface area of 0.047 m^2 g^{-1}) is estimated at 2 mL. This leads to a glass surface-to-liquid volume (S/V) ratio of 23500 m^{-1} for all experiments. The glass powder size was judiciously chosen to avoid its complete dissolution, the monoliths were introduced to facilitate the solid phases analyses. Blank experiments, with only the COx argillite, were also run to follow the concentration of the glass tracer elements (Mo, Cs, B, Li) in the outlet solutions. The data from of the blank experiments were subtracted from the data obtained in experiments with the clay, glass and/or steel to allow calculations of glass dissolution rates. A summary of the experiments can be seen in Table 4.

The percolation of COx pore water solution through the cell was assured with an operating pressure of 120 bars under CO_2 atmosphere (1% CO_2: 99% N_2). A Gilson 307 5SC HPLC pump (Lewis Center, Ohio, USA) was used to maintain a fixed pressure, inducing a flow rate between 0.05 and 0.38 mL d^{-1}. The cell was placed at room temperature until water saturation of the clay pores and the dead volume of the reactor before being placed in the oven at 50 or 90 °C. Considering that reaction rates of glass and steel are much lower at room temperature than at 50 or 90°C, the alteration time was considered to start after placing the reactors in the oven. The outlet solutions were collected in plastic vials fitted with a septum. For each sampling the vial with the leachate was removed and replaced by an empty clean vial. This allows the measurement of instantaneous concentration between two measurements (from t_i to t_{i+1}). The pH was immediately measured after each sampling. Solutions were filtered using a Whatman inorganic membrane filter with pore size about 0.2 mm and acidified with ultra-high-purity concentrated HNO_3 (2%). The vials were finally flushed with nitrogen to exclude air and then stored at 4°C before analyses.

At the end of each experiment, the percolation cells were removed from the oven and left to cool down for 24 hours at room temperature while keeping their ends closed. Because of the very high pressure used during the experiments, which causes a swelling of the claystone, a piston press was used to extract the clay cores. The samples were stored in vials purged with argon to minimize possible oxidation. They were then analysed by electron microscopy and Raman spectroscopy. The remaining samples were then kept in a glove box under inert atmosphere.

Sample solution analyses were achieved using ICP-MS for B, Li, Cs, Mo, Si, Mg^{2+}, Na^{+}, K^{+} and Ca^{2+}; Ion Chromatography for SO_4^{2-} and HR-ICP-MS for $^{29}Si/^{28}Si$ ratio. The morphological overview and the chemical analyses of the corroded glass and steel surfaces were performed using SEM coupled with an energy-dispersive X-ray spectrometer (EDX). Corrosion products were identified by micro-Raman spectroscopy. The set of analytical techniques and the instruments used are detailed in [20].

2.2. *LA-HR-ICP-MS $^{29}Si/^{28}Si$ isotope ratios of COx argillite cores*

$^{29}Si/^{28}Si$ isotope ratios were measured using a laser ablation device (UP-213, New Wave Research Inc., Huntingdon, Cambridgeshire, UK) coupled to a single-collector high resolution ICP-MS instrument (ELEMENT XR, Thermo Scientific, Bremen, Germany). The HR-ICP-MS was synchronized with the laser ablation device in external trigger mode. The laser system is equipped with a standard ablation cell. The laser settings were as follow: Energy output: 0.4mJ, Frequency: 10Hz, ablation mode: single spot, spot diameter: 90µm, dwell time: 50s and washout delay: 75s. Silicon isotopes ^{28}Si and ^{29}Si were measured using a triple mode detector setup and a medium mass resolution of 4000 in order to resolve spectral interferences.

Helium at a flow rate of 0.87l/min was used as carrier laser aerosol and argon at a flow rate of 0.9l/min was added just prior to ICP. A total analysis time of 2 mins was used to record time-integrated ^{28}Si and ^{29}Si signals of laser ablation sample (60s) and gas blank (60s). The HR-ICP-MS instrument was tuned for highest sensitivity on NIST SRM612 glass reference material while keeping a $^{238}U/^{232}Th$ ratio close to 1 and a $^{232}Th^{16}O/^{232}Th$ ratio below 0.1%. Two COx argillite cores located on both sides of the system (G-S-C-90°C-inlet side ; G-C-S-90°C-outlet side) with each side measuring 21 mm was cut and fixed onto an rounded epoxy mount with a double sided adhesive disc. $^{29}Si/^{28}Si$ isotope ratio profiles were measured using 20-22 single spots with a spacing between spots of 1.3 mm in the claystone matrix and 0.2 mm near the interface for a better resolution. $^{29}Si/^{28}Si$ isotope ratio profile of sample was bracketed with five analyses of the NIST SRM612. ^{28}Si and ^{29}Si isotope signals from the sample were corrected for gas blank measurements performed after sample laser ablation. Ten replicates of the NIST SRM612 measured twice during acquisition the same day of both COx argillite cores displayed $^{29}Si/^{28}Si$ isotope ratio averages and two standard deviations of the mean equal to 0.0515±0.0002 (G-S-C-90°C-inlet side) and 0.0515±0.0001 (G-S-C-90°C-outlet side). The average calculated value for the NIST SRM612 is used for calculating the

$\delta^{29}Si$ (‰) delta notation expressed with the following relationship $\delta^{29}Si=[(^{29}Si/^{28}Si)_{sample}/(^{29}Si/^{28}Si)_{NIST612}-1]\times100$. Calculated $\delta^{29}Si$ for the ^{29}Si-doped inactive simulated French nuclear waste glass SON68 is equal to 208.

2.3. Data treatment

The normalized concentration NC_i in g m^{-3} was calculated from the concentration of glass elements released into the leachate, using the formula:

$$NC_i = \frac{C_i}{X_i} \qquad (2)$$

With C_i the concentration of the element i in the leachate in gm^{-3} and X_i is the weight fraction of element i in the pristine glass.

The normalized dissolution rate NLR_{i+1} in g m^{-2} d^{-1} was calculated from two consecutive samplings according to the following expression:

$$NLR_{i+1} = \frac{\left(\frac{NC_i - NC_{i+1}}{(t_{i+1} - t_i)}\right) + \left(\frac{F}{V} \times NC_{i+1}\right)}{\frac{S}{V}} \qquad (3)$$

with i and $i+1$ two consecutive sampling intervals, t the alteration time in day, F the flow rate in m^3 d^{-1}, V the solution volume in m^3 and (S/V) the ratio of glass surface area to volume of solution in m^{-1}.

Analytical uncertainty of NLR was calculated from the standard deviation δ_f of the function $f(x1, x2,...,xn)$ and the standard deviation δ_i of the parameter i using the formula:

$$\delta_f = \sqrt{\sum_{i=1}^{n} \left(\frac{\partial f}{\partial x_i}\right)^2 \delta_i^2} \qquad (4)$$

The substitution of equation (3) into (4) gives:

$$\frac{\Delta NLR}{NLR} = \sqrt{\frac{\left[\Delta NC_t^2 + \Delta NC_{t+1}^2 + \left(\frac{F}{V} \times NC_{t+1}\right)^2 \left[\left(\frac{\Delta F}{F}\right)^2 + \left(\frac{\Delta V}{V}\right)^2 + \left(\frac{\Delta NC_{t+1}}{NC_{t+1}}\right)^2\right]\right]}{\left(\frac{NC_t - NC_{t+1}}{((t-1)-t)} + \frac{F}{V} \times NC_{t+1}\right)^2} + \left(\frac{\Delta V}{V}\right)^2 + \left(\frac{\Delta S}{S}\right)^2} \qquad (5)$$

In our set of experiments, the resulting errors were generally near 17% and were dependent mostly on the errors associated with the element concentrations in the leachate.

3. Results

3.1. Evolution of pH and ion concentrations in the leachate

The pH values of the outlet solutions, measured at 25°C, for the different percolation cells are shown in Fig. 2. For the experiment conducted at 50°C, the pH stabilizes towards a value close to 7. This low value of pH is due to the low dissolution of the glass at 50°C compared to the experiments conducted at 90°C; the pH remains therefore close to that imposed by the claystone (7.2 at 25°C). At 90°C, the pH is higher, which can be attributed to the dissolution of the glass, favourable at high temperatures. It can also be seen from the (G–C–S–90 °C) experiment that the pH stabilizes around 8, this value is about 0.5 units higher than in the (G–C–90°C) experiment without steel. The increase in pH in the first case is due to the production of hydrogen gas and the hydroxide ions following steel corrosion. Under anoxic conditions, steel corrosion occurs through the reduction of water:

$$2H_2O + 2e^- \longrightarrow H_{2(g)} + 2OH^-$$

The global equation of steel corrosion by water can therefore be written as:

$$Fe + 2H_2O \longrightarrow Fe^{2+} + 2OH^- + H_{2(g)}$$

Maintaining the highest pH values up to 583 days for the (G–C–S–90°C) experiment shows that the steel is not fully oxidized after this period. The pH is thus controlled by both the glass dissolution and iron corrosion but also the buffering capacity of the claystone.Fig. 2(a)–(e) shows the evolution with time of the concentrations of alkaline and alkaline-earth ions (Na^+, Mg^{2+}, Ca^{2+} and K^+), and sulphate ions SO_4^{2-} in the outlet solutions for the different percolation cells. At the beginning of the alteration, the ion concentrations in the outlet solutions are very high compared to their initial concentrations in COx water, this is observed for all experiments including the blank tests. The higher initial concentrations may be explained by a partial desaturation of the clay core by water evaporation during the storage leading to concentration increase of the remaining pore water. The concentrations then tend to stabilize from 150 days. This phenomenon has also been shown by Neeway [19] in percolation experiments using only COx clay.

The sodium concentration stabilizes around its initial value in COx water (inletsiderite concentration) for all experiments. The same was observed for Mg in (G–C–50°C) and (G–C–90°C) experiments. However, in (G–C–S–90°C) experiment the Mg concentration is on the order of 10 ppm, *i.e*. 5.6 times lower than the initial concentration in COx water at 90°C (55.9 ppm). This can be explained by the precipitation of this element with Si in the form of magnesium silicates. This phase has already been observed in batch reactor, it is formed at pH 8 for a temperature of 90 °C [10] [21] [22]. The sorption of dissolved silica on alteration products is often described as a responsible for the low concentration of Si in the leachate. Nevertheless, the behaviour of Mg also suggests that a part of Si is precipitated as magnesium silicates. In addition to this phase, analyses by Raman spectroscopy reveal a possible precipitation of magnesium sulphates.

The calcium concentration is lower than that in the COx water for the three experiments, it is even lower for (G–C–S–90°C) experiment. The drop in calcium concentration could be due to the calcite ($CaCO_3$) formation frequently observed in this type of experiment but also to its precipitation in the gel layer. The low concentration of calcium in the presence of steel may also result in precipitation of (Fe, Ca) carbonate [23]. The authors studied the corrosion of steel in the presence of clay at 90°C. They have indeed observed the existence of calciated siderite (siderite partly substituted by calcium, (Fe, Ca) CO_3) for which a certain number of Ca atoms (maximum 20%) replaces the Fe atoms. The formation of powellite ($CaMoO_4$) may explain the drop in Mo concentrations that accompany the drop of Ca. Fig. 2 (d) shows that the claystone continues to release K, indicating the dissolution of K-rich clays such as illite. The concentrations of this element, initially absent in pristine glass, seem to stabilize around 65 ppm. This value is higher than in COx water (36 and 39 ppm at 90 and 50 °C, respectively).

The concentrations of the sulphate ions stabilize around values equal to those in COx water for the experiments at 50 and 90 °C without steel. For (G–C–S–90 °C) experiment, the concentration of SO_4^{2-} is almost two times lower than that in (G–C–90 °C) experiment. It is difficult to assume a massive reduction of sulphates despite the formation of mackinawite (FeS) and pyrite (FeS_2) (see section 3.4), but the precipitation of magnesium sulphates may be responsible for the decrease in the concentration of sulphate ions.

3.2. Evolution of Si concentration and $^{29}Si/^{28}Si$ isotope ratio in the leachate

The evolution of Si concentration in the leachate for the different percolation cells is plotted as a function of time in Fig. 3(a). Si concentrations stabilize between 13 and 20 ppm for experiments conducted at 90°C and at 7 ppm for the experiment conducted at 50°C. These two concentrations are close to the concentrations resulting from the clay dissolution experiments at these two temperatures [24][25]. It appears therefore that the claystone controls the concentrations of silicon in solution. However, in the presence of steel, the silicon concentration is lower compared to the experiment without steel at 90°C. This difference between Si concentrations can be distinguished from 100 days of alteration.

The decrease in Si concentration in the presence of steel is likely due to: (1) the formation of iron silicates, this phase has been identified by SEM/EDX and Raman spectroscopy at the glass/steel and steel/clay interfaces for both inlet and outlet sides of alteration solution. This result is corroborated by the study of De Combarieu et al. [2], which revealed the precipitation of silicate phases that tend to consume Si and increase the dissolution rate of the glass; (2) the sorption of Si on corrosion products such as magnetite and siderite (identified by SEM/EDX and Raman spectroscopy).

Fig. 3(b) illustrates the evolution as a function of time of the $^{29}Si/^{28}Si$ isotope ratio in the outlet solutions for the different percolation cells. For (G–C–50 °C) experiment, the $^{29}Si/^{28}Si$ ratio remained constant throughout the experiment at the natural isotope ratio (0.0508). The same was observed for the other two experiments at 90 °C up to 200 days. $^{29}Si/^{28}Si$ isotope ratios then increased rapidly to stabilize around 0.096 for (G–C–90°C) experiment and 0.11 for (G–C–S–90°C) experiment.

The fact that the $^{29}Si/^{28}Si$ ratio does not change at 50°C shows that all the silicon released from the glass is retained in the clay cores. The advective/diffusive transport of silicon from the glass to the outlet of the reactor will then take more than 600 days. Silicon present in the aqueous phase can indeed interact with the clay in different ways: adsorption of orthosilicic acid (H_4SiO_4) at clay edge sites, nucleation/growth of new solid phases, or structural transformation of the initial clay. It should also be noted that the rate of SON68 glass alteration at 50°C is lower than at 90°C. In addition, the Si migration, governed by diffusion, advection and retention, is faster at 90°C than at 50°C. The increase of the $^{29}Si/^{28}Si$ ratio in the presence of steel may be explained by the reaction of the steel, released during the corrosion of the steel, with the argillite thus reducing the exchanges between ^{29}Si released from the glass and the clay. Alternatively, steel corrosion and concomitant formation of iron

silicates as corrosion products may lead to consumption of pre-existing natural Si in the pore water leading to accumulation of a larger fraction of Si in the pore water originating from the dissolving glass.

3.3. Evolution of $^{29}Si/^{28}Si$ isotope ratio in COx argillite cores

Figure 4 corresponds to an image of the system prepared for analysis with the HR-ICP-MS. The value of δ^{29}Si (%) as a function of position in COx argillite cores are reported in Fig. 5 together with the iron abundance expressed as the $^{56}Fe/^{27}Al$ ratio, where Al exists in the COx argillite while its concentration in the steel is very minor. Fig. 5a shows the δ^{29}Si (%) from the inlet side of the cell until the interface between clay and the steel powder and Fig. 5b exhibits the δ^{29}Si (%) from the steel powder through the COx argillite to the outlet side. The Fe abundance in the profiles of Fig. 5c and d makes it possible to locate the clay and the glass powder to perform the analyses, which has been difficult to identify under the microscope of the ICP-MS. The δ^{29}Si (%) of the clay is stable with no enrichment with regard the NIST SRM612 glass reference material having a natural $^{29}Si/^{28}Si$ isotope ratio. Nevertheless, the last data point from Fig. 5a, likely corresponding to the interface between the clay and the steel powder, shows a slight enrichment in Si-29 with regards the NIST SRM612 (δ^{29}Si = 5%) due to a contribution from the highly Si-29 enriched corroded steel powder (δ^{29}Si = 180%) (Fig. 5b). In fact, a contribution of only 2% from the steel leads to an increase of the δ^{29}Si from natural background to about 5%. Fig. 5b shows that the δ^{29}Si of the steel powder (180%) is very close to that of the pristine glass (208%), which clearly indicates that the Si released from the glass immediately reacts with the iron to form precipitates but also could adsorb onto corrosion products and only a small fraction of Si in the corrosion products corresponds to the pre-existing Si in flowing groundwater. This is the first time we show a strong sorption of Si released from the glass in the corrosion products in an integral system containing glass and near field materials.

3.4. Evolution of normalized leaching rates and effect of temperature and steel *on the glass alteration.*

The normalized dissolution rates of the glass tracers for the different percolations cells are plotted versus time in double logarithmic graphs in Fig. 6(a)–(c). Numerical results obtained between 525 and 583 days may be seen in Table 5. The volume of solution in contact with the glass is assumed to be 2 mL. The curves of the normalized leaching rate of elements seem to

follow the same trend. It can be noted that the release rates of B and Li are similar in all cases. After 525 days of alteration, the glass dissolution rate in the presence of clay at 90°C is around 5.5×10^{-3} g m^{-2} d^{-1} (Fig. 6(b)). This value is close to that obtained in the percolation cell at 90°C with the addition of steel for the same period (Fig. 6(c)). Mo shows relatively low release rates, this tendency has already been observed during the alteration of SON68 glass in batch and in dynamic mode under silica saturated COx water and without claystone [21]. Unlike (G–C–90°C) experiment, the release rate of Mo in (G–C–S–90°C) experiment is significantly low compared to B and Li (about 1 order of magnitude). This can be explained by the sorption of this element on the steel corrosion products (siderite and magnetite), or the precipitation of Mo-rich phase (calcium or barium molybdate).

The normalized dissolution rates of boron as a function of time for the different percolations cells can be seen in Fig. 6(d). The glass dissolution rate at 50°C is approximately one order of magnitude less than those measured at 90°C (2.7×10^{-4} g m^{-2} d^{-1} after 576 days). The presence of steel did not increase the glass dissolution for the same temperature (90°C) despite the retention of a fraction of silicon on the corrosion products. This suggests that the silica/steel and/or the silica/corrosion products interactions could be limited to the space around the steel/clay interfaces and do not prevent the reaching of silica concentration close to saturation in the zone in contact with the glass. This suggestion is reinforced by comparing the boron release rates obtained in these experiments with those obtained previously by Bouakkaz et al. [21] in batch reactor under silica saturated COx water ([Si] = 42 ppm) and in the absence of claystone (Fig. 6(e)). In all the experiments run at 90°C, the release curves of boron show similar trends. In all cases, glass dissolution rates continue to decrease linearly with time and the decrease seems to follow a slope of -0.5, suggesting a possible diffusion-controlled mechanism of glass alteration for longer periods of time.
The calculated alteration depths for the dissolution rates based on boron concentration (by dividing the normalized concentration NC by the glass density d = 2.63) are given in Fig. 6f. The maximum depth did not exceed 2 µm after more than 5 days of alteration.

3.5. Analyses of different interfaces by SEM/EDX and Raman spectroscopy.

MEB/EDX and Raman spectroscopy analyses were performed at the various interfaces for (G–C–S–90 °C) experiment after 583 days of alteration. The steel powder was found almost intact on both sides (inlet + outlet) and that of glass slightly cemented. The analyses show the existence of a large number of corrosion products of steel and glass. The steel corrosion,

either in monolith or powder form, leads mainly to the formation of magnetite (Fe_3O_4), siderite ($FeCO_3$) and iron sulphides. The presence of steel near the glass has a great impact on the morphology and structure of the alteration products of the glass. Fig. 7 shows a SEM/EDX image obtained on the surface of a glass monolith in contact with steel on the inlet side of the system. The corresponding Raman spectrum allows distinguishing the siderite mineral. This phase was identified at the glass/steel and steel/clay interfaces on both sides (inlet + outlet).

The Raman spectrum of siderite is characterized by an intense band around 1091 cm^{-1} attributed to the symmetric stretching ν_1 mode of carbonate groups. The internal vibration mode $\nu_4CO_3^{2-}$ of carbonate ions is located at 723 cm^{-1}. The network modes of siderite $FeCO_3$ are located at 169 and 294 cm^{-1} [26]. The corresponding EDX spectrum shows the incorporation of calcium in siderite. This tendency has already been observed by Schlegel et al. [23] during the corrosion of steel in the presence of clay at 90°C. Ca and/orMg $FeCO_3$-type iron carbonates have also been identified by El Mendili et al. [27] on the surface of steel in contact with clay at 30°C under CO_2 atmosphere. The incorporation of calcium in the siderite corroborates the solution analyses, where the calcium concentration is lower for the experiment with the presence of steel. Some studies highlight the formation of another type of iron carbonate with the chemical formula $Fe_2(OH)_2CO_3$ also called chukanovite. This mineral has been observed during the alteration of the steel in anoxic medium and for a neutral or slightly alkaline pH [28][29]. Despite favourable conditions, chukanovite could not be observed in this work. This can be explained by: (1) the high solubility of chukanovite compared to siderite [30], or (2) the high carbonate concentration that favours siderite formation rather than chukanovite [28]. In an aqueous medium rich in CO_3^{2-}, chukanovite can indeed be considered as a reaction intermediate leading to the formation of siderite according to the following mechanism [23][31]:

$$Fe_2(OH)_2CO_{3\,(s)} + CO_3^{2-}{}_{(aq)} \rightarrow 2FeCO_{3(s)} + 2OH^-{}_{(aq)}$$

In addition to siderite, another type of steel corrosion product has been identified at the glass/steel and steel/clay interfaces on both sides (inlet + outlet). It is magnetite which forms a layer on the surface of the metal. The magnetite may also form a layer on the surface of the glass in contact with the metal as shown in Fig. 8, where a glass powder in contact with steel powder (outlet side) is covered with a layer of magnetite. Raman spectrum shows the presence of characteristic vibrational modes of powellite (Fig. 8a) and magnetite (Fig. 8b). The Raman spectrum of powellite is characterized by the strongest peak at 879 cm^{-1} which

corresponds to the symmetric stretching ν_1 mode of internal [MoO_4] vibration in crystalline $CaMoO_4$. That of magnetite is characterized by vibration modes A_{1g} at 668 cm^{-1}, E_g at 306 cm^{-1}, and T_{2g} at 193 cm^{-1}. The absence of the mode at 1375 cm^{-1}, which corresponds to the magnon mode present in the γ-Fe_2O_3 maghemite phase, shows that the reactions occur under anaerobic conditions.

Powellite was often observed at the glass/steel interface on both sides of the cell, and infrequently inside the glass powder (away from the steel). It can also be noted that Mo is present in small amounts in siderite and magnetite as shown by EDX spectra of these two phases (Fig. 8(b) and 8(b)). This explains the low release rate of Mo (about 1 order of magnitude) compared to B and Li in (G–C–S–90 °C) experiment, which is not the case for (G–C–90 °C) experiment. This result is corroborated by the study conducted by Verbinnen et al. [32] that reveals the sorption of Mo on magnetite.

The alteration of glass in the presence of steel also gives rise to the formation of silicate phases. SEM/EDX and Raman analyses show the precipitation of ferrosilicates at the glass/steel interface (Fig. 9). This secondary phase, consuming silicon, can increase the dissolution affinity of the glass and thus control its residual rate. It was observed during the glass alteration in the presence of steel at 90°C [2], as well as at 50°C [11]. The precipitation of ferrosilicates often coincides with a strong alteration of the glass due to silica concentration decrease in solution. Furthermore, ferrosilicates precipitation consumes silica naturally present in ground waters [24]. Consequently, the formation of ferrosilicates stimulates to some extent the development of thick gel layers at the glass surface.

Amorphous silica was identified at the glass/steel interface. The precipitation of the latter was envisaged by Inagaki et al. [4] to explain the decrease in Si content in the leachate during the alteration of nuclear glass in the presence of steel corrosion products. The amorphous silica may also precipitate on the clay surface either as spherical flaky nodules, or in the form of coatings on the clay surface [33]. The decrease in Si concentration for (G–C–S–90 °C) experiment observed in Fig. 3(a) can therefore be attributed to three major phenomena: (1) the formation of Fe-silicate; (2) silicon sorption on the corrosion products such as magnetite and siderite; and (3) the precipitation of pure silica at the glass/steel interface. Furthermore, the increase in the local pH at the glass/steel interface involves the precipitation of Mg silicates, which form at pH 8 and at 90°C [22]. This explains the decrease in the concentration of Mg in the presence of iron (Fig. 2(b)). The Raman spectrum of Mg silicate shows the presence of the

modes at 115 and 187 cm^{-1} assigned to Mg–OH vibrations, the peaks at 436 and 677 cm^{-1} were attributed to Si–O–Si bending.

In addition to silicate phases, the presence of apatite ($Ca_5(PO_4)_3(OH)$) is observed. This phase was frequently observed at the glass/steel interface on both sides of the system (inlet + outlet), but also inside the glass powder away from the steel. The Raman spectrum of this phase is characterized by the presence of many phosphate (PO_4^{3-}) vibration modes, in particular the strongest one at 967 cm^{-1} which corresponds to the symmetric ν_1 stretching mode. At locations not covered by precipitates, alteration gel can be observed indicating a homogeneous flow of the leaching solution through the cell and perfect contact with the glass powder.

Fig. 10(a-c) shows SEM/EDX image of a glass grain in contact with steel on the inlet side of the cell. The Raman spectrum obtained shows the presence of the main Raman vibrational bands: A_g (379 cm^{-1}), E_g (343 cm^{-1}) and $3T_g$ (430 cm^{-1}) characteristics of pyrite FeS_2. This phase was also identified on the surface of the steel powder in contact with the clay on both sides of the cell. Pyrite is known to originally exist in the COx clay but also could neoform at low temperature via microbiological activity [34][35].

Other categories of iron sulphide have been identified by Raman spectroscopy at the glass/steel and steel/clay interfaces. It concerns pyrrhotite (FeS_{1+x}), troilite (FeS) and mackinawite ($Fe_{1+x}S$) (Fig. 10(d)). The presence of these iron sulphides at this temperature is likely due to the reduction of the pyrite originally present in the clay by hydrogen produced by steel reductive oxidation. Pyrite is a potential oxidizer of hydrogen due to the degree of oxidation (-1) of sulphur, which can be reduced to S (-2). Thermodynamically, the reduction of pyrite to pyrrhotite or troilite with the formation of H_2S is possible [36]:

$$FeS_2(s) + H_2(aq) \rightarrow FeS(s) + H_2S(aq)$$

$$FeS_2(s) + (1\text{-}x)\, H_2(aq) \rightarrow FeS_{1+x}(s) + (1\text{-}x)\, H_2S(aq) \qquad (0 < x < 0.13)$$

When the pyrrhotite is low in sulphur ($0 < x < 0.10$), it has a hexagonal crystal structure; when it is rich in sulphur ($0.09 < x < 0.13$), it has a monoclinic phase which is weakly magnetic. Pyrrhotite rarely exists as a pure phase, it is generally a mixture of hexagonal and monoclinic phases. El Mendili et al. [29] showed that pyrite was partially reduced by hydrogen to iron monosulphide under alkaline conditions at 90°C. The reduction of pyrite leads to the production of H_2S which contributes to an increase in steel dissolution and to the formation of

mackinawite $Fe_{1+x}S$ ($0.89 < x < 1$). This phase has been identified by Raman spectroscopy at the glass/steel and steel/clay interfaces. Even though the formation of steel corrosion products increases its dissolution *via* H_2S production, the layer may further develop, protecting the metal surface, when the formed corrosion products are dense and slightly soluble [37]. A theoretical evaluation of the solubility values of the different iron sulphide phases gives pKs values of 2.95 ± 0.1 for poorly crystallized iron sulphides; 3.6 ± 0.2 for mackinawite; 5.1 ± 0.1 for pyrrhotite and 16.4 ± 1.2 for pyrite [38][39]. When iron sulphide forms a continuous film on the metal surface, it acts as a protector. If the film is discontinuous, localized corrosion occurs [40].

Although the vibrational modes of all iron monosulphide phases have not been previously described in the literature, a Raman spectrum of pyrrhotite formed in deep-sea hydrothermal environments has been proposed by Breir et al. [41]. Their spectrum is similar to ours with intense bands around 220, 325, 390 and 475 cm^{-1}. Even if no Raman bands were assigned by the authors, their results have been confirmed by chemical analyses. Avril et al. [42] proposed the Raman spectrum of troilite found in a meteorite. Their spectrum shows vibration modes at 160, 290 and 335 cm^{-1} with sometimes an additional peak at 240 cm^{-1}. The four fundamental vibration modes of mackinawite were identified and assigned by El Mendili et al. [40]: 228 cm^{-1} (B_{1g}), 256 cm^{-1} (E_g), 376 cm^{-1} (A_{lg}) and 395 cm^{-1} (E_g). Raman spectra obtained on precipitates present at the glass/steel interfaces correspond to magnesium sulphate $MgSO_4$ [43], calcium sulphate $CaSO_4$ [44] and calcite $CaCO_3$ [45] (Fig. 10(e)). The presence of these precipitates near the iron explains the decrease in magnesium, calcium and sulphate concentrations for (G–C–S–90 °C) experiment observed in Fig. 2(b,c,e). The precipitation of sulfate, originally present in the COx water, indicates their slow reduction kinetic even in the presence of reducing environment in the percolation cell, in particular near the steel powder.

MEB/EDX and Raman spectroscopy analyses for (G–C–50 °C) experiment after 576 days of alteration revealed the presence of calcite and Mg-silicates in both glass/clay interface and inside the glass powder. The same phases in addition to apatite and powellite were observed for (G–C–90 °C) experiment after 525 days of alteration. The different phases observed at the various sites for (G–C–S–90 °C) experiment after 583 days of alteration are listed in Table 6.

Conclusion

Percolation tests conducted with the SON68 glass at 50 and 90°C in the presence of COx clay with/without steel showed continuously decreasing reaction rates and no noticeable effect of the presence of steel on glass dissolution. This contrasts many other studies at much higher water/solid ratio, showing increase of glass corrosion rates in presence of steel corrosion products. After more than 500 days of runs, the dissolution rate is slightly lower in the presence of steel powder [G–S–C–90°C: 2.8 (±0.4)×10^{-3} g m^{-2} d^{-1}] than in the absence [G–C –90°C: 5.5 (±0.8)×10^{-3} g m^{-2} d^{-1}]. Nevertheless, the steel corrosion had led to silica retention in corrosion products (ferrosilicates). Co-precipitation of Si with Fe was confirmed by the surface characterization of the corrosion products as well as by the HR-ICP-MS analysis of isotopic silicon profile of the percolation cell. The precipitation of amorphous silica indicates high saturation conditions reached near the glass/steel interface, which helps keeping a low glass dissolution rate evolving toward a final constant rate. The precipitation of reducing steel corrosion products (magnetite, siderite) together with the formation of pyrite-reduction products in the presence of hydrogen (pyrrhotite, mackinawite) indicates reducing conditions favourable for maintaining low solubilities of actinides and the majority of fission products like Tc or Se. Furthermore, the formation of apatite and powellite is expected to contribute into actinides stabilisation via co-precipitation. For the long-term prediction of glass dissolution via geochemical modelling further studies could include better characterization of ferrosilicates and Mg-silicates with higher space resolution at the various interfaces.

Acknowledgement

We thank Andra for the partial financial support of this work. We are thankful to Dr. S. Gin from the French Alternative Energy and Atomic Energy Commission (CEA) for providing the doped glass. We thank also Nicolas Stephan from the Institut des Matériaux de Nantes Jean Rouxel (Nantes, France) for his help with SEM analyses.

Data availability

The raw/processed data required to reproduce these findings cannot be shared at this time as the data also forms part of an ongoing study.

References

[1]. Ledieu, F. Devreux, P. Barboux, L. Sicard, O. Spalla, Leaching of borosilicate glasses. I. Experiments, J. Non-Cryst. Solids. 343 (2004) 3–12.

[2]. G. De Combarieu, M.L. Schlegel, D. Neff, E. Foy, D. Vantelon, P. Barboux, S. Gin, Glass– iron–clay interactions in a radioactive waste geological disposal: An integrated laboratory-scale experiment, Appl. Geochem. 26 (2011) 65–79.

[3]. Abdelouas, W. Lutze, E. Nuttall, W. Gong, Remediation of U (VI)-contaminated water using zero-valent iron. C.R.A.S. Series IIA Earth Plan. Sci. 5 (1999) 315–319.

[4]. Y. Inagaki, A. Ogata, H. Furuya, K. Idemistu, T. Banba, T. Maeda, Effects of Redox Condition on Waste Glass Corrosion in the Presence of Magnetite, *Mater. Res. Soc. Symp. Proc.* 412 (1996) 257–264.

[5]. S. Ben Lagha, D. Crusset, I. Mabille, M. Tran, M.C. Bernard, E. Sutter, Corrosion of iron: A study for radioactive waste canisters, J. Nucl. Mater. 362 (2007) 485–492.

[6]. H. El Hajj, A. Abdelouas, B. Grambow, C. Martin, M. Dion, Microbial corrosion of P235GH steel under geological conditions, Phys. Chem. Earth. 35 (2010) 248–253.

[7]. H. El Hajj, A. Abdelouas, Y. El Mendili, G. Karakurt, B. Grambow, C. Martin, Corrosion of carbon steel under sequential aerobic–anaerobic environmental conditions. Corros. Sci. 76 (2013), 432–440.

[8]. Y-M. Pan, V. Jain, O. Pensado, Degradation of high-level waste glass under simulated repository conditions, J. Non-Cryst. Solids. 319 (2003) 74–88.

[9]. C. Mayant, B. Grambow, A. Abdelouas, S. Ribet, S. Leclercq, Surface site density, silicic acid retention and transport properties of compacted magnetite powder. Phys. Chem. Earth 33 (2008), 991–999.

[10]. N. Godon, S. Gin, D. Rebiscoul, P. Frugier, SON68 glass alteration enhanced by magnetite, Proc. Earth. Plan. Sci. 7 (2013) 300–303.

[11]. E. Burger, D. Rebiscoul, F. Bruguier, M. Jublot, J.E. Lartigue, S. Gin, Impact of iron on nuclear glass alteration in geological repository conditions: a multiscale approach, Appl. Geochem. 31 (2013) 159–170.

[12]. Michelin, E. Burger, E. Leroy, E. Foy, D. Neff, K. Benzerara, P. Dillmann, S. Gin, Effect of iron metal and siderite on the durability of simulated archeological glassy material, Corros. Sci. 76 (2013) 403–414.

[13]. P. De Cannière, H. Moors, A. Dierckx, F. Gasiaux, M. Aertsens, M. Put, P. Van Iseghem, Diffusion and Sorption of ^{32}Si-labelled silica in the boom clay. Radiochim. Acta 82 (1998) 191–196.

[14]. S. Gin, P. Jollivet, J.P. Mestre, M. Jullien, C. Pozo, French SON68 nuclear glass alteration mechanisms on contact with clay media, Appl. Geochem. 16 (2001) 861–881.

[15]. K. Lemmens, The effect of clay on the dissolution of nuclear waste glass, J. Nucl. Mater. 298 (2001) 11–18.

[16]. P. McGrail, W. L. Ebert, A. J. Bakel, D. K. Peeler, Measurement of kinetic rate law parameters on a Na–Ca–Al borosilicate glass for low-activity waste, J. Nucl. Mater. 249 (1997) 175–189.

[17]. E. C. Gaucher, C. Lerouge, P. Blanc, C. Tournassat, Caractérisation géochimique des forages PAC et nouvelles modélisations, THERMOAR. BRGM/RP–5446–FR, 2007.

[18]. Gaucher E, Robelin C, Matray JM, et al. ANDRA underground research laboratory: Interpretation of the mineralogical and geochemical data acquired in the Callovian-Oxfordian formation by investigative drilling. Phys Chem Earth 29 (2004) 55–77.

[19]. Jougnot, A. Revil, P. Leroy, Diffusion of ionic tracers in the Callovo-Oxfordian clay-rock using the Donnan equilibrium model and the formation factor, Geochim. Cosmochim. Acta. 73 (2009) 2712–2726.

[20]. J.J. Neeway, The alteration of the SON 68 reference waste glass in silica saturated conditions and in the presence of water vapor. PhD thesis, University of Nantes, 2011.

[21]. R. Bouakkaz, A. Abdelouas, Y. El Mendili, B. Grambow, S. Gin, SON68 glass alteration under Si-rich solutions at low temperature (35–90 °C): kinetics, secondary phases and isotopic exchange studies, RSC. Adv. 5 (2016) 64538–64549.

[22]. M. Debure, P. Frugier, L. De Windt, S. Gin, Borosilicate glass alteration driven by magnesium carbonates, J. Nucl. Mater. 420 (2012) 347–361.

[23]. M.L. Schlegel, C. Bataillon, C. Blanc, D. Prêt, E. Foy, Anodic activation of iron corrosion in clay media under water-saturated conditions at 90°C: characterization of the corrosion interface. Environ. Sci. Technol. 44 (2010) 1503–1508.

[24]. T. Suzuki-Muresan, J. Vandenborre, A. Abdelouas, B. Grambow, Solution controls for dissolved silica at 25, 50 and 90 °C for quartz, Callovo-Oxfordian claystone, illite and MX80 bentonite, Phys. Chem. Earth. 36 (2011) 1648–1660.

[25]. J.J. Neeway, A. Abdelouas, S. Ribet, Y. El Mendili, S. Schumacher, B. Grambow, Effect of Callovo-Oxfordian clay rock on the dissolution rate of the SON68 simulated nuclear waste glass, J. Nucl. Mater. 459 (2015) 291–300.

[26]. S.K. Sharma, A.K. Misra, S.M. Clegg, J.E. Barefield, R.C. Wiens, T.E. Acosta, D.E. Bates, Remote-Raman spectroscopic study of minerals under supercritical CO_2 relevant to Venus exploration, Spectrochim. Acta. Part. A. 80 (2011) 75–81.

[27]. Y. El Mendili, A. Abdelouas, A. Aït Chaou, J.F. Bardeau, Carbon steel corrosion in clay-rich environment, Corros. Sci. 88 (2014) 56–65.

[28]. M. Saheb, Les analogues archéologiques ferreux pour la compréhension des mécanismes de corrosion multiséculaire en milieu anoxique, PhD thesis, University of Paris-Est, 2009.

[29]. Y. El Mendili, A. Abdelouas, G. Karakurt, A. Aït Chaou, R. Essehli, J.F. Bardeau, J.M. Grenèche, The effect of temperature and microbial activity on carbon steel corrosion under simulated geological conditions, Appl. Geochem. 52 (2015) 76–85.

[30]. Azoulay, C. Remazeilles, Ph. Refait, Determination of standard Gibbs free energy of formation of chukanovite and Pourbaix diagrams of iron in carbonated media, Corros. Sci. 58 (2012) 229–236.

[31]. T.R. Lee, R.T. Wilkin, Iron hydroxy carbonate formation in zerovalent iron permeable reactive barriers: characterization and evaluation of phase stability, J. Contam. Hydrol. 116 (2010) 47–57.

[32]. B. Verbinnen, C. Block, P. Lievens, A. Van Brecht, C. Vandecasteele, Simultaneous Removal of Molybdenum, Antimony and Selenium Oxyanions from Wastewater by Adsorption on Supported Magnetite, Waste. Biomass. Valor. 4 (2013) 635–645.

[33]. Pozo, O. Bildstein, J. Raynal, M. Jullien, E. Valcke, Behaviour of silicon released during alteration of nuclear waste glass in compacted clay, Appl. Clay. Sci. 35 (2007) 258–267.

[34]. C. Rémazeilles, M. Saheb, D. Neff, E. Guilminot, K. Tran, J.A. Bourdoiseau, R. Sabot, M. Jeannin, H. Matthiesen, P. Dillmann, P. Refait, Microbiologically influenced corrosion of

archaeological artefacts: characterisation of iron(II) sulfides by Raman spectroscopy, J. Ram. Spect. 41 (2010) 1425–1433.

[35]. Y. El Mendili, A. Abdelouas, H. El Hajj, J.F. Bardeau, Phase transitions of iron sulphides formed by steel microbial corrosion. RSC Advances 3 (48) (2013) 26343–26351.

[36]. W. Lee, W.G. Characklis, Corrosion of Mild Steel Under Anaerobic Biofilm, Corros. 49 (1993) 186–199.

[37]. D.R. Bush, Sodium Sulphides. Kirk-Othmer Encyclopedia of Chemical Technology, 2000.

[38]. W. Davison, N. Philips, B.J. Tabner, Soluble iron sulfide species in natural waters: Reappraisal of their stoichiometry and stability constants, Aquat. Sci. 61 (1999) 23–43.

[39]. L.G. Benning, R.T. Wilkin, H.L. Barnes, Reaction pathways in the Fe–S system below 100°C, Chem. Geol. 167 (2000) 25–51.

[40]. Y. El Mendili, B. Minisini, A. Abdelouas, J.F. Bardeau, Assignment of Raman-active vibrational modes of tetragonal mackinawite: Raman investigations and Ab-Initio Calculations, RSC. Adv. 4 (2014) 25827–25834.

[41]. J.A. Breier, C.R. German, S.N. White, Mineral phase analysis of deep-sea hydrothermal particulates by a Raman spectroscopy expert algorithm: Toward autonomous in situ experimentation and exploration, Geochem. Geophys. Geosyst. 10 (2009) 1525–2027.

[42]. C. Avril, V. Malavergne, R. Caracas, B. Zanda, B. Reynard, E. Charon, E. Bbobocioiu, F. Brunet, S. Borensztajn, S. Pont, M. Tarrida, F. Guyot, Raman spectroscopic properties and Raman identification of CaS-MgS-MnS-FeS-Cr_2S_3 sulfides, Meteorit. Planet. Sci. 48 (2013) 1415–1426.

[43]. W.W. Rudolph, G. Irmer, G.T. Hefter, Raman spectroscopic investigation of speciation in $MgSO_4$(aq), Phys. Chem. Chem. Phys. 5 (2003) 5253–5261.

[44]. S.N. White, Laser Raman spectroscopy as a technique for identification of seafloor hydrothermal and cold seep minerals, Chem. Geol. 259 (2009) 240–252.

[45]. H.G.M. Edwards, S.E. Jorge Villar, J. Jehlicka, T. Munshi, FT–Raman spectroscopic study of calcium-rich and magnesium-rich carbonate minerals, Spectrochim. Acta. Part A. 61 (2005) 2273–2280.

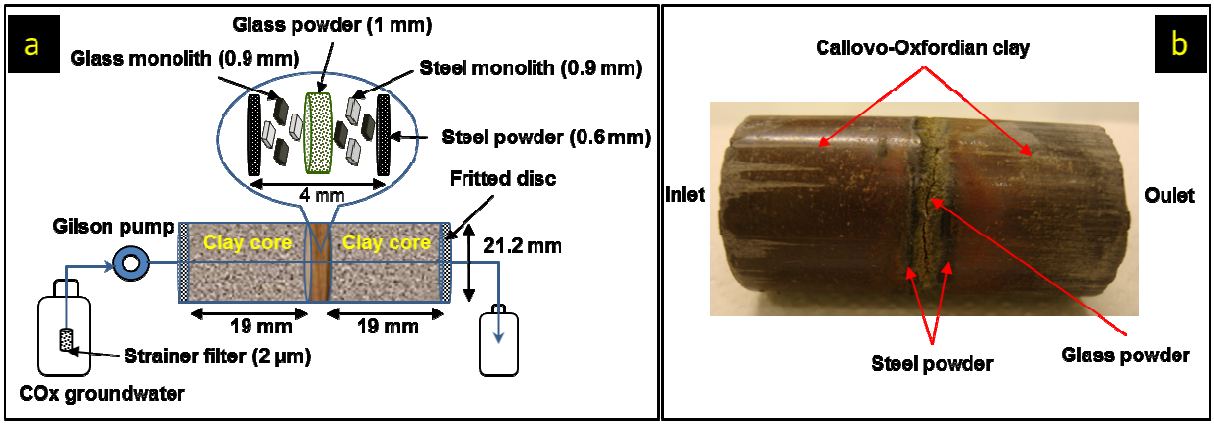

Fig. 1. (a) A detailed representation of the percolation experiment to study the system (G–C–S–90 °C). For the system (G–C) the same organization is used without addition of iron. (b) An image of the experimental setup after dismantlement.

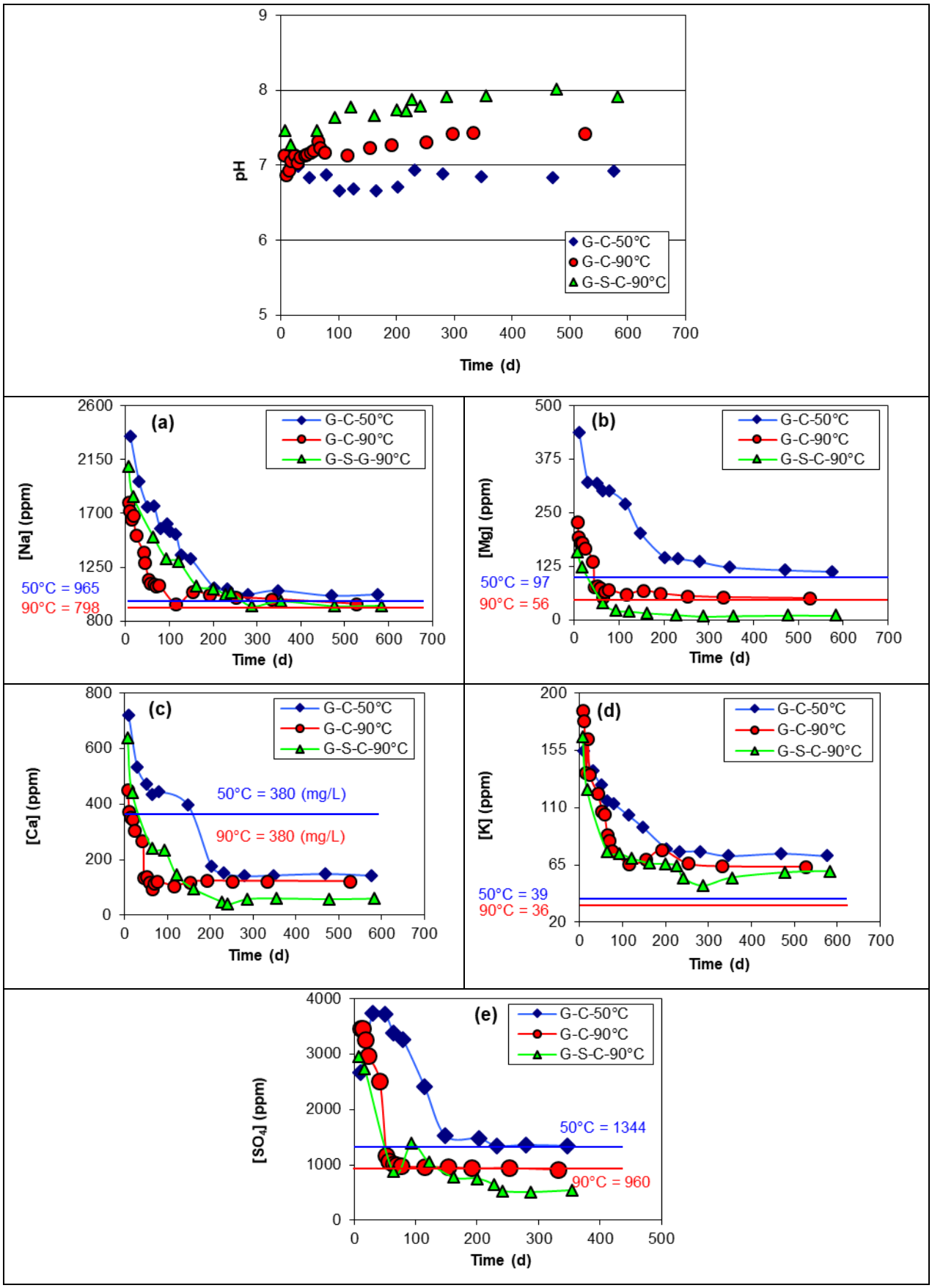
pH
Time (d)
G-C-50°C
G-C-90°C
G-S-C-90°C
(a)
[Na] (ppm)
G-S-G-90°C
50°C = 965
90°C = 798
(b)
[Mg] (ppm)
50°C = 97
90°C = 56
(c)
[Ca] (ppm)
50°C = 380 (mg/L)
90°C = 380 (mg/L)
(d)
[K] (ppm)
50°C = 39
90°C = 36
(e)
[SO4] (ppm)
50°C = 1344
90°C = 960

Fig. 2. Evolution with time of pH (measured at 25°C), Na^+ (a), Mg^{2+} (b), Ca^{2+} (c), K^+ (d) and SO_4^{2-} (e) concentrations for the different percolation cells. The horizontal lines correspond to the initial concentrations of the element in the inlet solutions (blue 50 °C, red 90 °C). Errors are about 10%. The pH in the blank experiment using only clay (blank experiment) stabilized at about 7.2 for 50°C and 6.5-7 for 90°C.

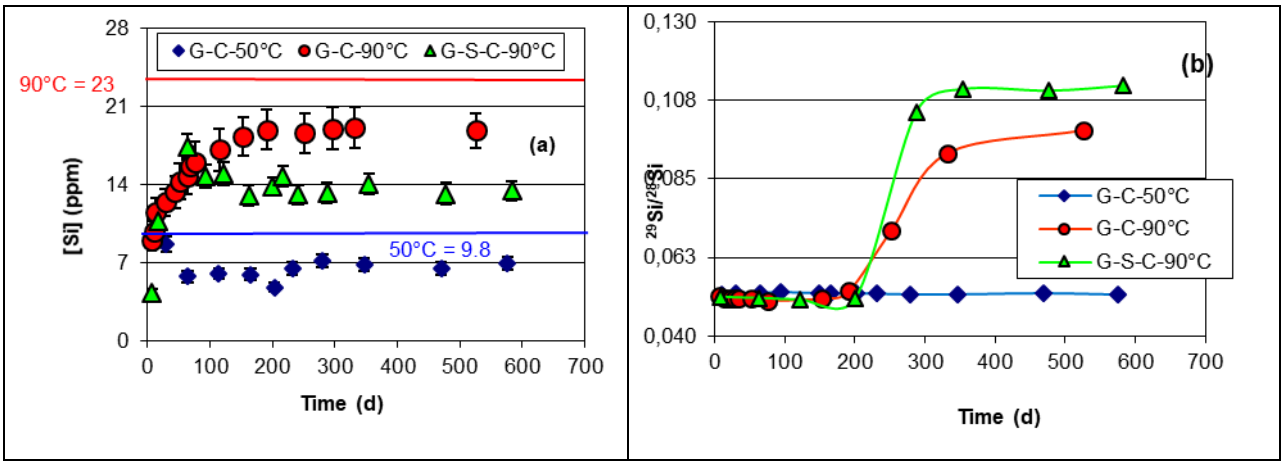

Fig. 3. Evolution with time of Si concentration (a) and the $^{29}Si/^{28}Si$ isotope ratio (b) in the outlet solutions for the different percolation cells. The horizontal lines correspond to the initial concentrations of Si in the inlet solutions (blue 50 °C, red 90 °C). Errors (2σ) are about 10% for [Si] and less than 2% for $^{29}Si/^{28}Si$ isotope ratio.

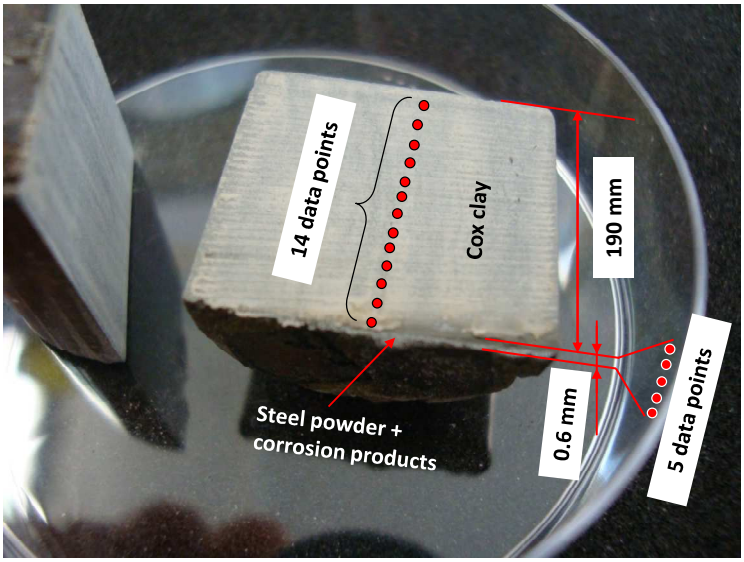

Fig. 4. Image of the outlet side of the percolation experiment longitudinally cut into half showing the steel powder and the COx clay and the location of the data points for HR-ICP-MS analyes.

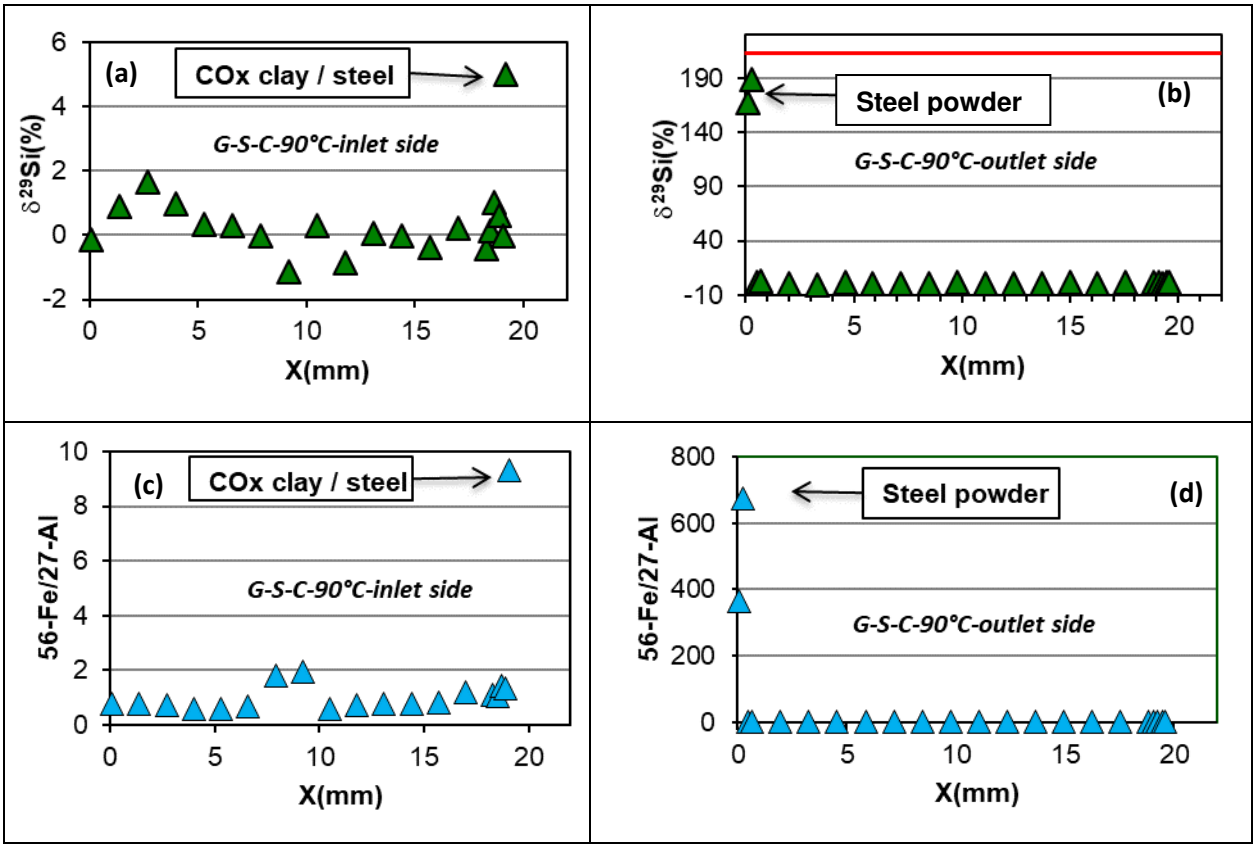

Fig. 5. $^{29}Si/^{28}Si$ isotope ratio profiles (a and b) and ^{56}Fe abundance expressed as $^{56}Fe/^{27}Al$ ratio (c and d) of two COx argillite cores located on both sides of the system (G-S-C-90°C-inlet side; G-S-C-90°C-outlet side). The $\delta^{29}Si$ of the glass used in the experiment equal to 208 is symbolized by the red line line (Fig.

5b). Two standard deviation of the mean calculated from ten replicates of NIST SRM612 for each $^{29}Si/^{28}Si$ profile analysis is used to propagate the error on the $\delta^{29}Si$ relationship. $\delta^{29}Si$ are reported with 0.3-0.4% error(2σ).

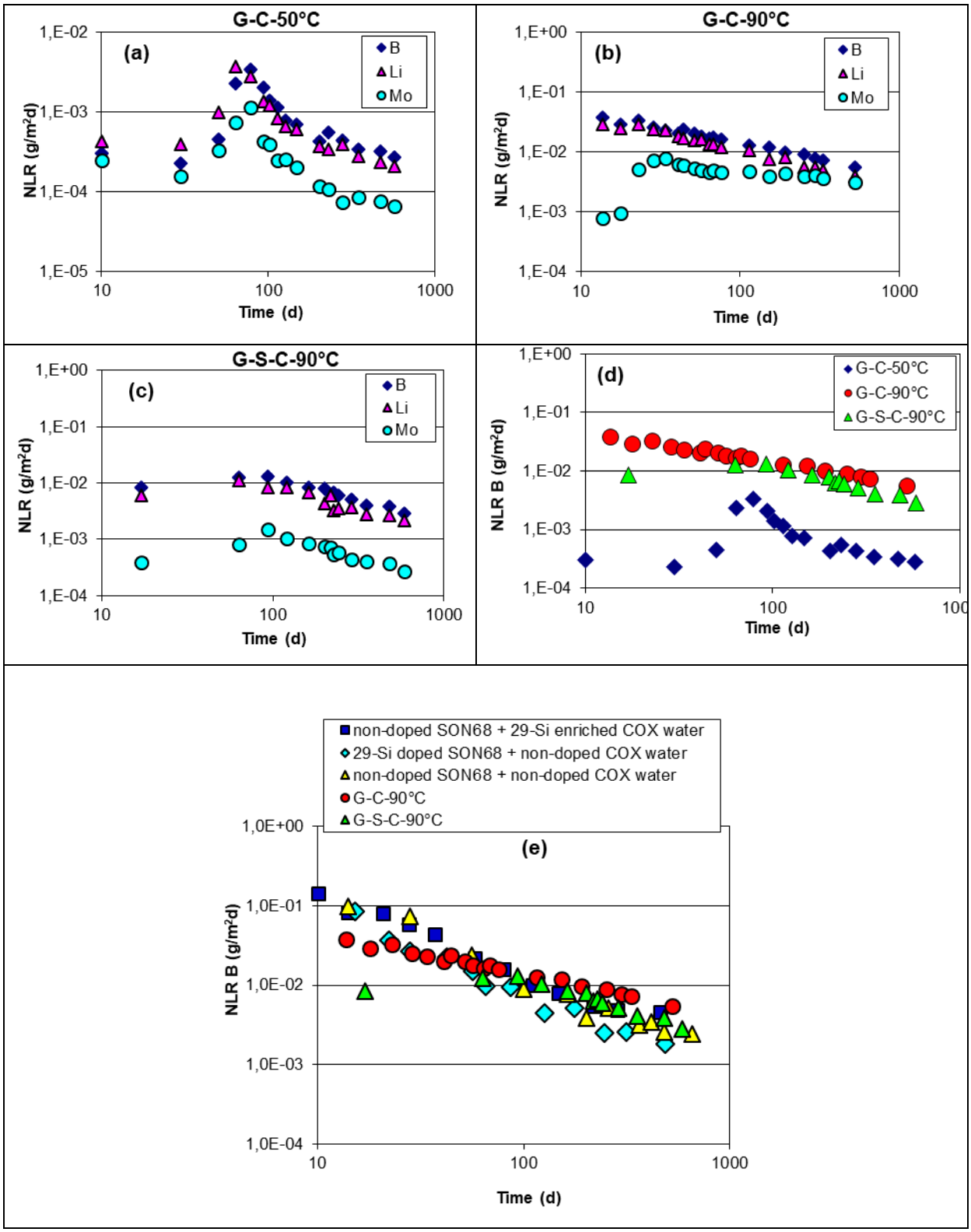

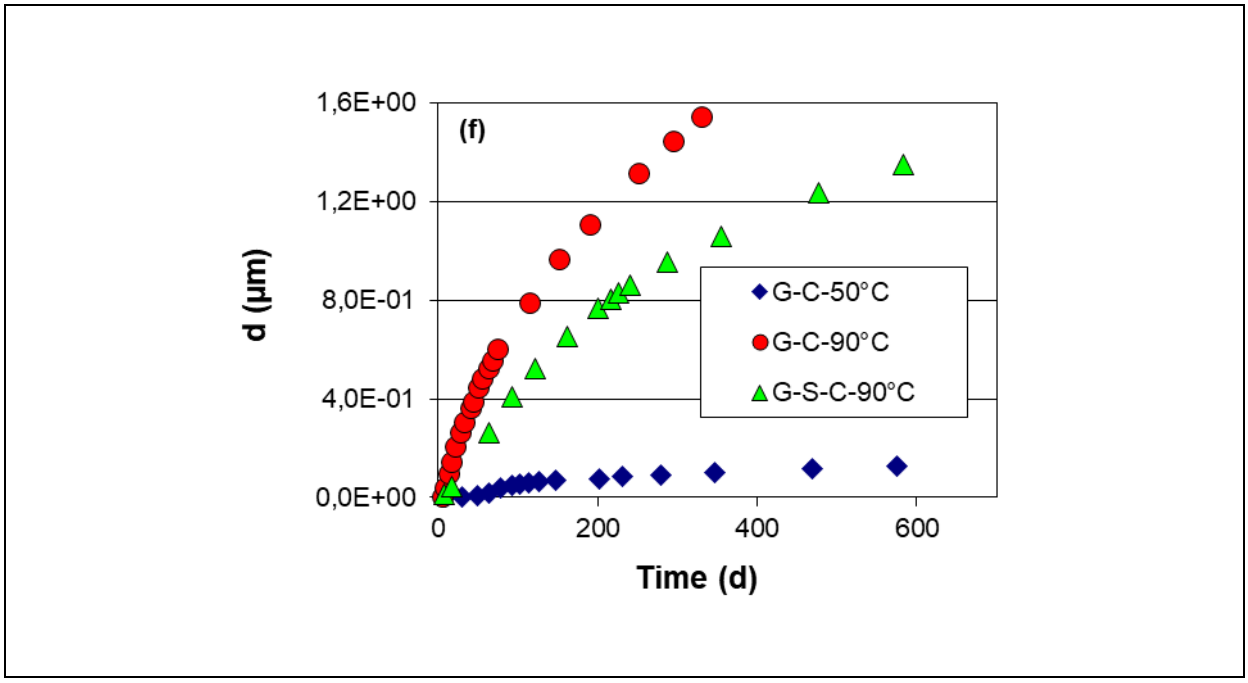

Fig. 6. (a-c) Evolution with time of normalized dissolution rates (NLR, g $m^{-2}d^{-1}$) of the glass tracers for the different percolations cells. (d) NLR of boron versus time for the different percolations cells. (e) A comparison of the NLR values based on boron release at 90°C for percolation experiments (this work) and other experiments run in batch under silica saturated COx water ([Si] = 42 ppm), pH 8, and in the absence of claystone [20]. Errors in NLR values are near 17%. (f) Alteration depths for the glass for different experimental conditions.

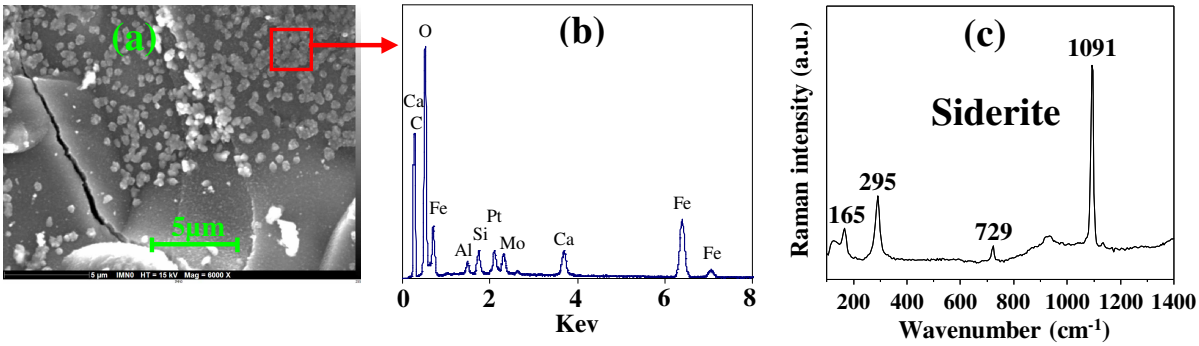

Fig. 7. SEM micrograph of the glass monolith surface in contact with steel on the inlet side of the system (G–S–C–90 °C) obtained for 583 days of alteration (a). The corresponding EDX (b) and Raman (c) spectra indicate the precipitation of siderite mineral $FeCO_3$.

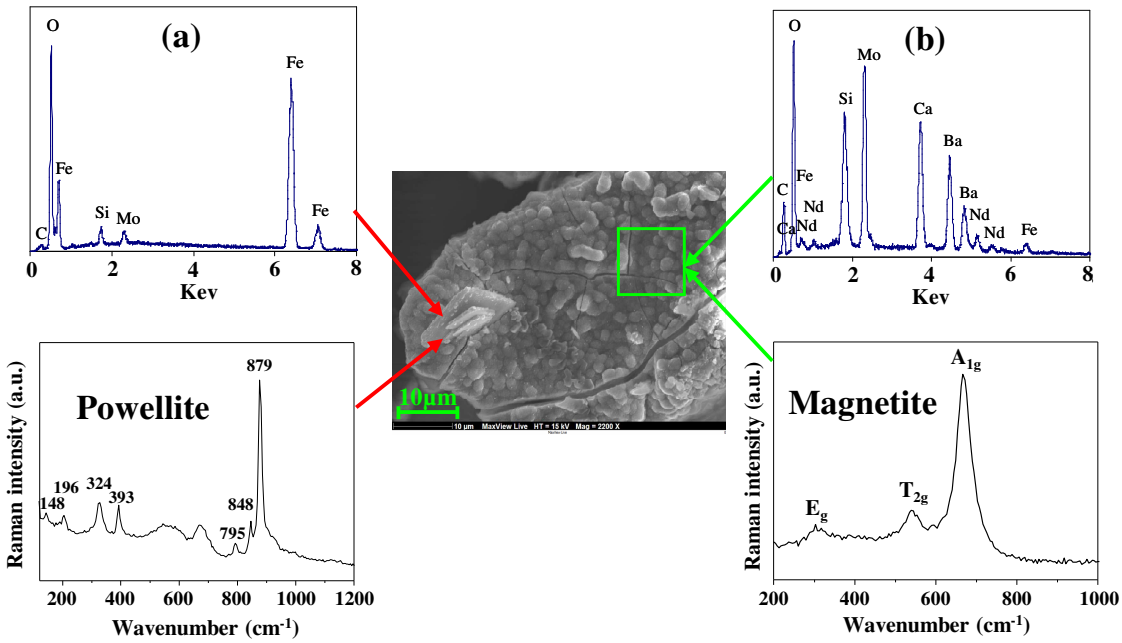

Fig. 8. SEM micrograph of SON68 glass powder in contact with steel on the outlet side of the system (G–S–C–90 °C) obtained for 583 days of alteration. The corresponding EDX and Raman spectra indicate the precipitation of powellite (a) and magnetite (b).

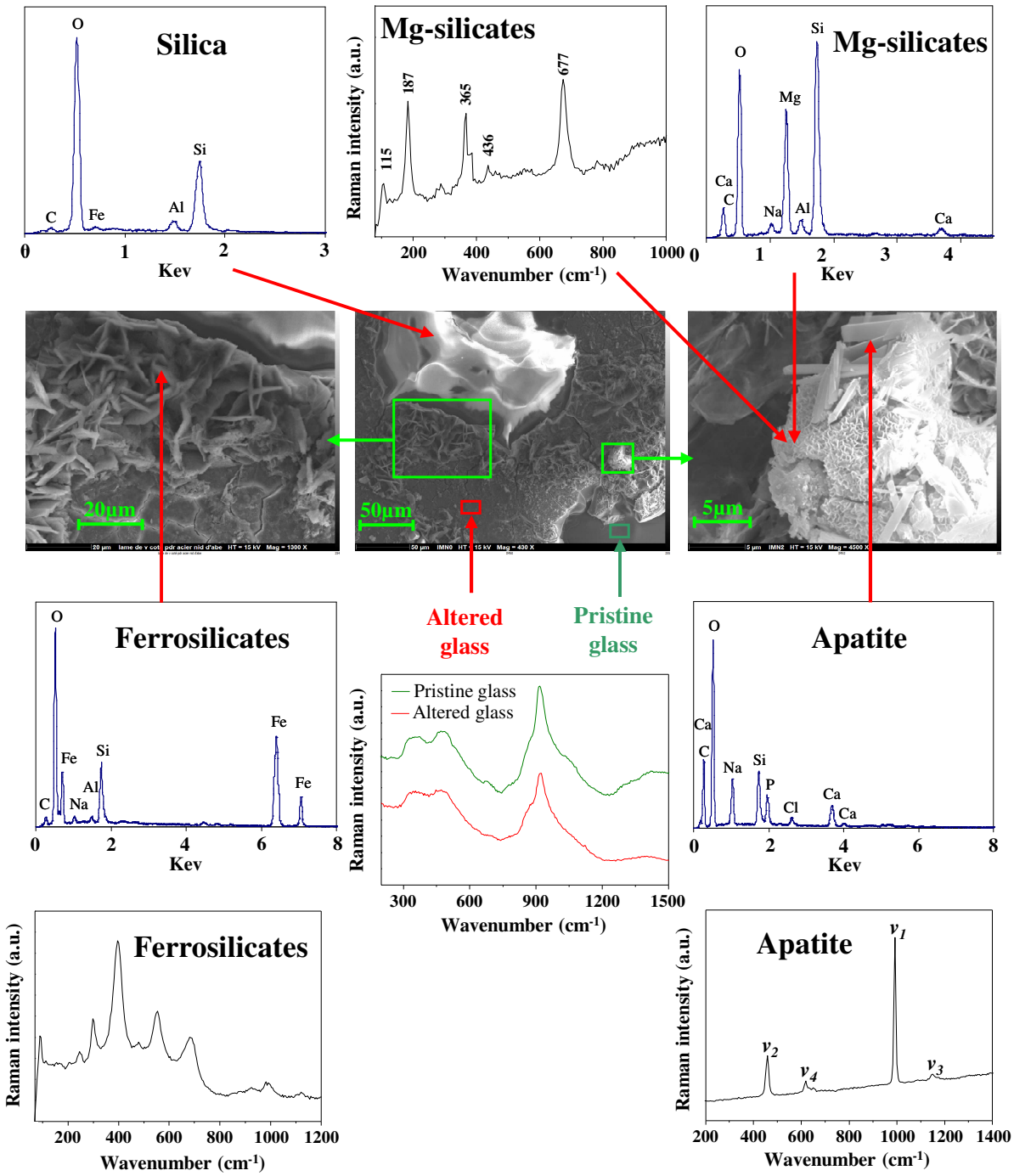

Fig. 9. SEM/EDX images and Raman spectra of SON68 glass monolith in contact with steel on the intlet side of the system (G–S–C–90 °C) obtained for 583 days of alteration, showing the precipitation of amorphous silica, Mg silicates, ferrosilicates and apatite.

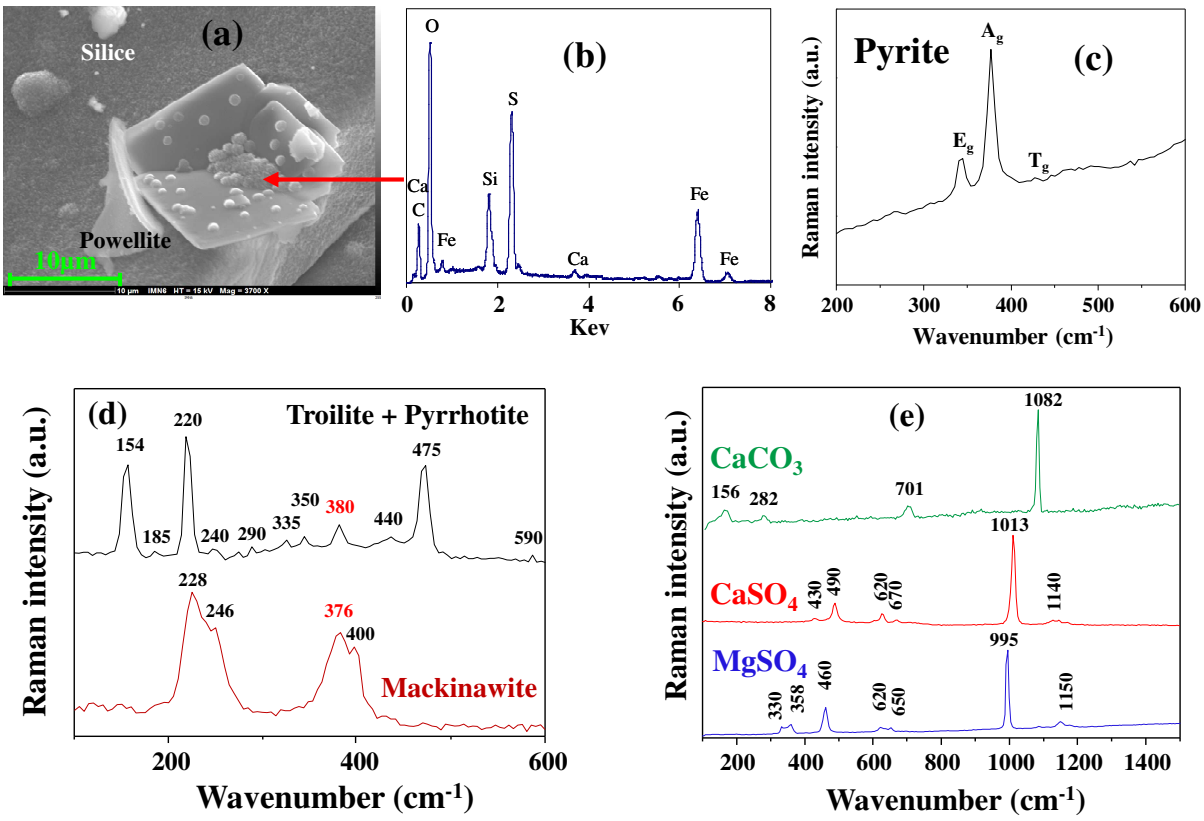

Fig. 10. SEM/EDX images and Raman spectra of SON68 glass powder in contact with steel on the inlet side of the system (G–S–C–90 °C) obtained for 583 days of alteration, showing the precipitation of amorphous silica, powellite, pyrite, troilite, pyrrhotite, mackinawite, calcite, Ca and Mg sulphates.

Table 1. Chemical composition in wt% of the inactive simulated French nuclear waste glass SON68.

Oxide	wt %	Oxide	wt %	Oxide	wt %
SiO_2	45.85	ZnO	2.53	Nd_2O_3	2.04
B_2O_3	14.14	P_2O_5	0.29	Pr_2O_3	0.46
Na_2O	10.22	SrO	0.35	Ag_2O	0.03
Al_2O_3	5.00	ZrO_2	2.75	CdO	0.03
CaO	4.07	MoO_3	1.78	SnO_2	0.02
Li_2O	1.99	Cs_2O	1.12	TeO_2	0.23
Fe_2O_3	3.03	BaO	0.62	Ce_2O_3	0.97
NiO	0.43	Y_2O_3	0.20	Others	0.39
Cr_2O_3	0.53	La_2O_3	0.93		

Table 2. Composition in weight% of P235GH stainless steel, designed for the manufacture of the overpack containers. The balance is Fe.

Element	wt%	Element	wt%
C	0.160	Ni	0.08
Mn	0.60-1.20	Mo	0.020
P	0.025	Nb	0.020
S	0.015	V	0.020
Si	0.35	Ti	0.030
Al	0.020	N	0.012
Cu	0.30	Ni+Cr+Cu+Mo	0.70
Cr	0.30		

Table 3. The chemical composition of COx water at 50 and 90°C [17].

	Concentration (mmol/L)	
Component	**50°C**	**90°C**
Cl^-	41	41
SO_4^{2-}	14	10
Na^+	42	39
K^+	1	0.96
Ca^{2+}	9.9	10
Mg^{2+}	4.1	2.5
Sr^{2+}	0.2	0.17
Si^{4+}	0.35	0.84
TIC	3.05	3.3

Table 4. Summary of the percolation experiments performed in this work.

Test	T (°C)	^{29}Si-doped SON68	P235GH steel	Saturation time at room temperature (days)	Alteration time (days)	Experiment period (days)
G–C	50	1g powder 4 monoliths	–	27	576	603
G–C	90	1g powder 4 monoliths	–	40	526	566
G–S–C	90	1g powder 4 monoliths	0.5 + 0.5 g powder 4 monoliths	62	583	645
Blank 1	50	–	–	51	585	636
Blanc 2	90	–	–	49	596	645

Table 5: Normalized release rates of glass elements in g $m^{-2}d^{-1}$ for the different percolations cells obtained between 525 and 583 days.

	NLR (g m^{-2} d^{-1})		
Element	G–C–50°C (576 days)	G–C–90°C (525 days)	G–S–C–90°C (583 days)
B	2.7 (±0.4) × 10^{-4}	5.5 (±0.8) × 10^{-3}	2.8 (±0.4) × 10^{-3}
Li	2.1 (±0.3) × 10^{-4}	3.9 (±0.6) × 10^{-3}	2.2 (±0.3) × 10^{-3}
Mo	6.7 (±1.1) × 10^{-5}	3.1 (±0.5) × 10^{-3}	2.7 (±0.4) × 10^{-4}

Table 6: The different phases observed at the various locations for (G–S–C–90 °C) experiment after 583 days of alteration.

Localisation	Observed phases
Glass/iron interface (inlet + outlet) sides	Siderite, Magnetite, Amorphous silica, Ferrosilicates, Hydrated glass, Mg silicates, Powellite, Apatite, Calcite, Pyrite, Pyrrhotite, Troilite, Mackinawite, $MgSO_4$ and $CaSO_4$
Iron/clay interface (inlet + outlet) sides	Siderite, Magnetite, Calcite, Pyrite, Pyrrhotite, Troilite and Mackinawite
Inside the glass powder	Hydrated glass, Mg silicates, Powellite, Apatite and Calcite